nature communications

Article

https://doi.org/10.1038/s41467-025-64073-y

All-fiber highly efficient delivery of 2 kW laser over 2.45 km hollow-core fiber

Received: 9 May 2025

Accepted: 8 September 2025

Published online: 09 October 2025

Check for updates

Jing Shi[1,2,5], Binyu Rao[1,2,5], Zilun Chen[1,2,5,6] ✉, Zefeng Wang[1,2,5,6] ✉, Guangrong Sun[1,2], Zuying Xu[3], Zhen Huang[1,2], Peng Li[4], Zihan Dong[4], Min Fu[1,2], Xin Tian[1,2], Baolai Yang[1,2], Jian Zhang[1,2], Zhiyue Zhou[1,2], Tianyu Li[1,2], Lei Zhang[4], Biao Shui[3], Chenxin Gao[1,2] & Jinbao Chen[1,2,6] ✉

Anti-resonant hollow-core fibers have emerged as an important medium for high-power laser delivery due to their low optical nonlinearity and high damage threshold. However, current delivery systems of high-power laser based on anti-resonant hollow-core fibers mainly rely on free-space optical components, which limits long-term stability. Here, we report an all-fiber delivery of 2 kW laser with 85.4% transmission efficiency over 2.45 km, using a self-fabricated hollow-core fiber with a record low transmission loss of 0.168 dB/km at 1080 nm. Notably, we observed the phenomenon of stimulated Raman scattering amplified within the silica nested tubes for the first time. By effectively suppressing the Raman noise from the laser source, we achieve an all-fiber laser delivery without stimulated Raman scattering of silica glass. This work marks a significant breakthrough in multi-kilometer and multi-kilowatt power delivery that is potentially useful for industrial manufacturing, nuclear decommissioning, laser drilling in oil and so on.

High-power fiber lasers have found extensive applications in industrial processing, medical biotechnology, and scientific research[1–3], owing to their prominent advantages including excellent beam quality, high conversion efficiency, compact structure, and effective thermal management. In recent years, fiber lasers have continuously developed[4–6], and significantly expanded their application domains. Meanwhile, there is a growing demand for the flexible long-distance delivery of high-power lasers. For instance, flexible long-distance high-power laser delivery systems enable physical separation between laser sources and workpieces, improving factory layout flexibility[3]. In nuclear decommissioning applications, such systems facilitate remote cutting of radioactive structures, significantly reducing radiation exposure risks[7]. For oil and gas exploration, the technology enables safer and more precise subsurface laser drilling operations, providing a sustainable alternative to conventional rock fragmentation methods[8]. However, conventional solid-core fibers (SCFs) for laser delivery are limited by the material damage threshold and nonlinear effects, which restrict further increases in transmission power and length. For example, the ytterbium-doped fiber laser developed by Fujikura Ltd. demonstrates a transmission length of 20 m at 5 kW output power[5], which decreases to 3 m when the power is increased to 8 kW[6]. Anti-resonant hollow-core fibers (AR-HCFs) provide a novel approach for addressing the limitations of SCFs[9–15], which emerges as an enabling tool for the flexible long-distance delivery of high-power lasers.

AR-HCFs confine the propagation of light within an air-filled core through a micro-structured cladding[14]. This design minimizes the overlap between the light field and the surrounding silica glass to approximately 10^{-5}, significantly reducing optical nonlinearity and enhancing the damage threshold[16,17]. Furthermore, with the development of AR-HCFs[18–22], the transmission loss of which has been

[1]College of Advanced Interdisciplinary Studies, National University of Defense Technology, Changsha, China. [2]Nanhu Laser Laboratory, National University of Defense Technology, Changsha, China. [3]Everfoton Technologies Corporation Limited, Wuhan, China. [4]State Key Laboratory of Optical Fiber and Cable Manufacture Technology, Yangtze Optical Fiber and Cable Joint Stock Limited Company (YOFC), Wuhan, China. [5]These authors contributed equally: Jing Shi, Binyu Rao, Zilun Chen, Zefeng Wang. [6]These authors jointly supervised this work: Zilun Chen, Zefeng Wang, Jinbao Chen. ✉e-mail: zilun2003@163.com; zefengwang_nudt@163.com; kdchenjinbao@aliyun.com

comparable to that of SCFs. In C-band, AR-HCFs have achieved an exceptionally low loss below 0.1 dB/km, establishing a new record[23]. Notably, the laser operating in the 1 μm spectral band represents the highest power level of fiber laser output, wherein existing literature documents a transmission loss of 0.3 dB/km for AR-HCF[24]. These combined properties render AR-HCFs particularly advantageous for flexible long-distance delivery of high-power lasers. Notable demonstrations include the delivery of 1 kW continuous laser over 1 km with a loss of 0.74 dB/km[25], narrow-linewidth laser delivery of 2.2 kW over 100 m with a loss of 0.79 dB/km[26], and 3 kW multimode laser delivery over 100 m with a loss of 3.27 dB/km[27] based on AR-HCFs in the 1 μm spectral band, proving the potential of AR-HCFs for flexible long-distance delivery of high-power lasers.

However, existing high-power laser delivery systems based on AR-HCFs mainly rely on free-space optical components[26–30], which limits long-term stability in dynamic environments. In addition, high-power laser delivery introduces thermal lensing effects, which affect coupling efficiency in spatial coupling[27]. In terms of all-fiber laser delivery system, a delivery of 100 W single-frequency laser power over a 100 m AR-HCF has been reported in 2024[31]. However, the coupling method relies on fiber alignment through a five-axis adjustment stage, which requires precise operation. Moreover, the coupling position reaches a temperature of 84.6 °C at an output power of 100.3 W, preventing its application in kilowatt-class laser delivery.

In this work, we demonstrate an all-fiber delivery of 2 kW laser with 85.4% transmission efficiency over a 2.45 km self-fabricated AR-HCF. This represents a record transmission distance for high-power laser delivery based on AR-HCFs. This achievement can be attributed to the following four key factors: Firstly, the AR-HCF achieves a record low transmission loss of 0.168 dB/km at 1080 nm; Secondly, a low-loss fusion splicing is developed between AR-HCFs and anti-reflection-coated SCFs; Thirdly, we observed the phenomenon of stimulated Raman scattering (SRS) amplified within the silica nested tubes of AR-HCF for the first time. By effectively suppressing the Raman noise from the laser source by utilizing a chirped and tilted Bragg grating (CTFBG), we achieve an all-fiber laser delivery without SRS of silica glass. Lastly, an end cap spliced with the output end of the AR-HCF protects the originally bare fiber facet from contamination and damage. The all-fiber integrated configuration constitutes a significant breakthrough, facilitating the transition of AR-HCF technology from the laboratory to practical applications.

Results

Fiber design and fabrication

The high-power laser source used in this work is a commercial laser source with a central wavelength of 1080 nm, utilizing a SCF of 20/250 μm (core/cladding diameter) as the output fiber, which supports two modes (LP_{01}/LP_{11}). In an all-fiber architecture, optimal coupling efficiency requires mode field matching between AR-HCFs and SCFs.

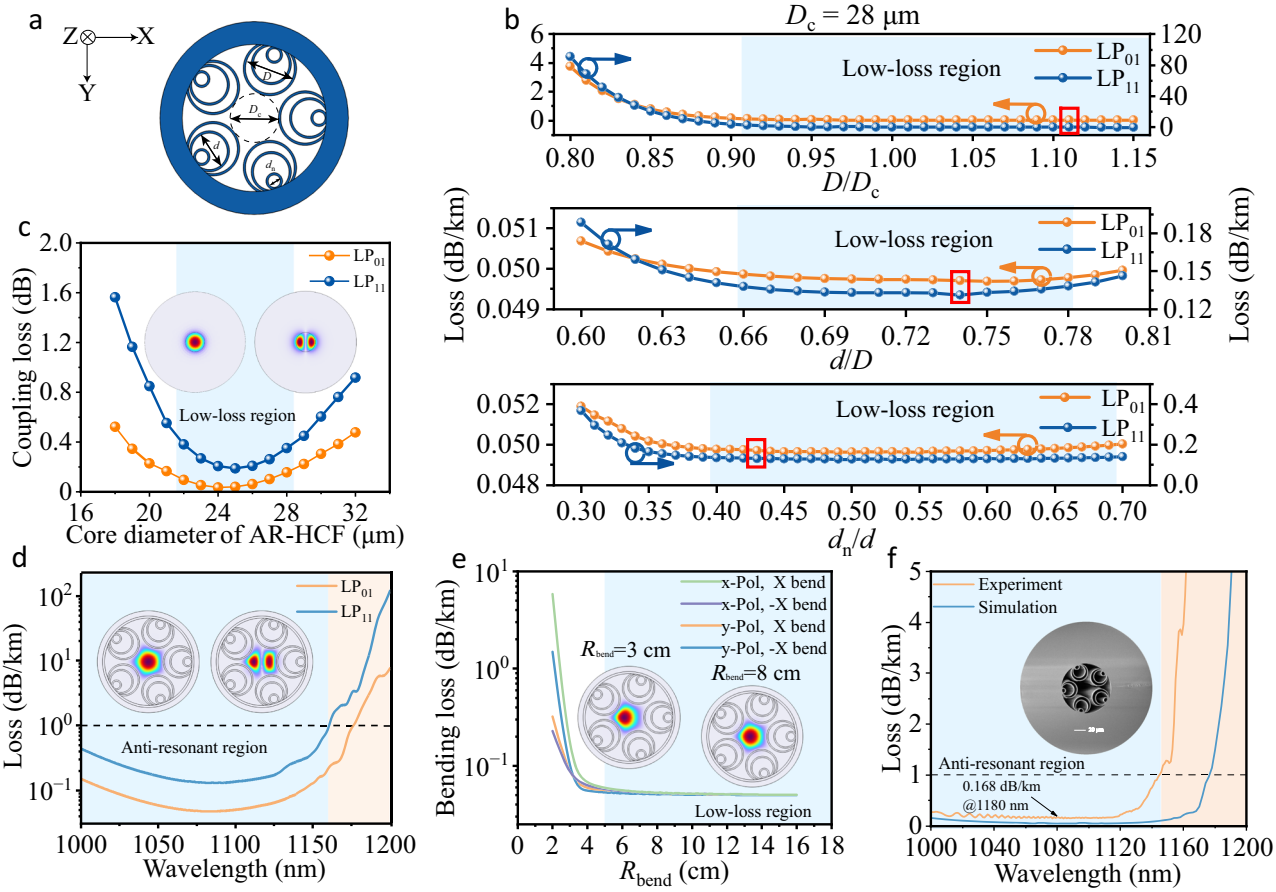

Fig. 1 | Characterization of the AR-HCF. a Cross section of the designed AR-HCF. **b** Simulated losses of the LP_{01} (orange line) and LP_{11} (blue line) modes as a function of D/D_c, d/D, and d_n/d, respectively, for the AR-HCF with a core diameter of 28 μm. The red box represents the actual parameters of the fabricated AR-HCF. **c** Simulated the coupling losses of the LP_{01} (orange line) and LP_{11} (blue line) modes between the SCF and the AR-HCF as a function of the core diameter of AR-HCF. Insets show the LP_{01} and LP_{11} mode-field profiles of the SCF. The blue regions show low-loss regions of the AR-HCF with a core dimeter of 22-28 μm. **d** Simulated losses of the LP_{01} (orange line) and LP_{11} (blue line) modes of the AR-HCF as a function of wavelength. The two insets show the mode-field profiles of LP_{01} and LP_{11} modes of the AR-HCF. **e** The bending loss of AR-HCF as a function of bending radius. The insets show the fundamental mode-field profiles of AR-HCF at bend radii of 3 cm and 8 cm, respectively. **f** Measured average transmission loss of the AR-HCF (orange line): from 1080 m to 20 m and from 1060 m to 20 m; simulated LP_{01}-mode transmission loss of the AR-HCF (blue line). The inset shows SEM image of the bare fiber cross-section.

Therefore, we designed an AR-HCF with a modal field matching with the SCF of 20/250 µm. Furthermore, the designed AR-HCF could exhibit low transmission losses for both the LP_{01} and LP_{11} modes to ensure efficient power delivery.

The five-tube nested AR-HCF exhibits broader anti-resonant bandwidth, lower transmission loss, and higher mode extinction ratio relative to designs incorporating six or more nested tubes[32]. This architecture previously achieved a record low transmission loss of 0.3 dB/km in the 1 µm spectral band[24]. In addition, recent studies indicate that increasing the number of nested tubes can effectively suppresses cladding-mode coupling, thereby reducing transmission loss[15]. Based on these studies, we designed a five-tube double-nested AR-HCF. The schematic diagram of the structure of the AR-HCF is shown in Fig. 1a, specifying the core diameter (D_c) and the diameters of the double-nested tubes (D, d, and d_n). We simulated the loss of the LP_{01} and LP_{11} modes considering leakage loss, bending loss, surface scattering loss and material absorption loss. To achieve low loss of the LP_{01} and LP_{11} modes in the AR-HCF, we conducted univariate optimization using systematic finite element analysis (FEA), as shown in Fig. 1b. It can be observed that when the parameter D/D_c satisfies greater than 0.9, the losses of the two modes stabilize. Furthermore, the modal losses exhibit a non-monotonic dependence on the scaling ratios between diameters of the adjacent tube: d/D and d_n/d, where an optimal range exists. Across the studied ranges ($0.66 \le d/D \le 0.78$, $0.39 \le d_n/d \le 0.69$), the LP_{01} and LP_{11} modes demonstrate losses below 0.05 dB/km and 0.14 dB/km, respectively. This occurs because undersized secondary/ tertiary layers weaken anti-resonant confinement, causing substantial optical leakage and increased propagation loss. Conversely, oversized layers make adjacent nested tubes too close, inducing resonances that degrade transmission performance and consequently increase transmission loss. The blue regions in Fig. 1b show the low-loss regions with optimal parameters, providing a relatively large range for drawing fibers. The red box represents the parameters of the fabricated AR-HCF.

Under high-power laser delivery, mode field matching is critical, as mode field mismatches can induce significant coupling loss, localized heating at fusion points, and even potential system failure. Figure 1c shows the coupling losses of the LP_{01} and LP_{11} modes between the SCF and the AR-HCF with core diameters of 18-32 µm. The coupling loss at the butt-coupled interface can be calculated as[33]

$$\alpha = -10\log_{10}\left(\frac{\left|\int \mathbf{E_i^*}\,\mathbf{E_t}\,dS\right|^2}{\int \mathbf{E_i^*}\,\mathbf{E_i}\,dS \int \mathbf{E_t^*}\,\mathbf{E_t}\,dS}\right) \quad (1)$$

Here, the vectors $\mathbf{E_i}$ and $\mathbf{E_t}$ represent the transverse electric fields of the fundamental mode in the SCF and the AR-HCF, respectively. The LP_{01} and LP_{11} mode-field profiles of the SCF and the AR-HCF were simulated, as shown in the insets of Fig. 1c, d. Due to the imperfect symmetry of the LP_{11} mode field in the five-tube nested AR-HCF, its coupling loss with the LP_{11} mode supported in SCF is higher than that of the LP_{01} mode. Simulations indicate that within the D_c range from 22 to 28 µm, the LP_{01} mode coupling loss is below 0.2 dB and the LP_{11} mode coupling loss is less than 0.4 dB. Theoretical analysis indicates that increasing the core diameter of AR-HCFs can effectively reduce the overlap between the mode field and the nested tubes, thereby suppressing the Raman gain coefficient (see Supplementary Note 5 for simulation results). Therefore, this study employs a core diameter of 28 µm. Table 1 shows the parameters of the fabricated AR-HCF. The thickness of the nested tubes is around 1.3 µm, which places the target wavelength of 1080 nm in the anti-resonance region of the third window[34].

Table 1 | Parameters of fabricated AR-HCF

D_c (µm)	D (µm)	d (µm)	d_n (µm)	D/D_c	d/D	d_n/d
28	31	23	10	1.1	0.74	0.43

The simulation result of the LP_{01} and LP_{11} mode losses is shown in Fig. 1d under fabricated parameters. The entire area in Fig. 1d is divided into an anti-resonant region (blue) where the LP_{01} and LP_{11} modes maintain losses below 1 dB/km, and a resonant region (orange). At the wavelength of 1080 nm, the loss of LP_{01} mode is ~ 0.05 dB/km, while the LP_{11} mode is ~ 0.13 dB/km. The insets in Fig. 1d show mode-field profiles of LP_{01} and LP_{11} core modes of the AR-HCF. Figure 1e presents the simulated bending losses for both x-polarization and y-polarization in the ±X-direction. The results demonstrate excellent bending resistance, with loss maintaining stability at bending radii ≥5 cm. The insets in Fig. 1e show simulated mode-field profiles of AR-HCF at bend radii of 3 cm and 8 cm. Figure 1f shows the average transmission loss, measured over lengths ranging from 1080 m to 20 m and from 1060 m to 20 m using the cutback method (see Methods) and the simulated LP_{01}-mode transmission loss of the AR-HCF. The bending radius of AR-HCF is 16 cm here. The anti-resonant region (blue) is defined where the transmission loss is below 1 dB/km. The results demonstrate a loss of 0.168 dB/km at 1080 nm, which is currently the record low-loss value in this spectral band. At 1142 nm, the loss of AR-HCF is 0.890 dB/km. Discrepancies in anti-resonant regions between simulation and experiment may stem from drawing-induced imperfections in nested tube uniformity.

Low-loss fusion splicing

Due to the different materials at the interface between SCFs and AR-HCFs (silica/air), back-reflected light induced by Fresnel reflection accounts for approximately 4% of the input power. Here, the anti-reflection coating method[35] was adopted to decrease the energy loss caused by Fresnel reflection.

The SCF was coated with a four-layer Ta_2O_5/SiO_2 film, and then the anti-reflection-coated SCF and the AR-HCF were spliced using a commercial fiber splicer. Figure 2 presents the experimental setup. In this setup, a 1060 nm narrow-linewidth fiber laser operating at an output power of 10 mW was utilized as the light source. The power of the AR-HCF output and the back-reflected light was monitored in real-time through power meters during the process of fiber splicing. The fusion splicing parameters were adjusted based on iterative testing. The transmission efficiency is calculated as the ratio between the input power (P_{in}) and the output power (P_{out}) of the AR-HCF. The return loss is derived from the input power (P_{in}) and the return power (P_{back}).

Experimental results demonstrate that discharge current and duration significantly influence splicing performance. Figure 2b provides a microstructural characterization of fusion-spliced fiber interfaces at relatively high, suitable, and low discharge parameters. Excessive discharge parameters induce thermal degradation of the anti-reflection coatings and collapse of the AR-HCF microstructure. Conversely, when discharge parameters are insufficient, the mechanical bonding at the fusion point is weak and easier to break, with no observable fusion traces remaining on the surface of the SCF. Through parameter optimization of discharge current and duration, we identified optimal splicing conditions for the SCF and the AR-HCF in this experiment: 20 mA discharge current and 600 ms duration. The corresponding cross-section views of post-splicing of SCFs and AR-HCFs are shown in the middle of the Fig. 2b. Notably, the distinct imprint of the nested tubes on the SCF surface matches that at the interface of the AR-HCF, with no observable coating delamination or thermal deformation. Anti-reflection coatings and nested tubes of the AR-HCF remain intact with a withstands tension load of ~400 g. Under the optimized parameters, five repeated splicing trials yielded an average insertion loss of ~0.17 dB (σ = 0.013 dB). The corresponding return loss measured ~ -28.5 dB (σ = 0.16 dB). Return loss characterization at 1080 nm is provided using a supercontinuum laser in Supplementary Note 1. The coupling losses align closely with simulated predictions, validating the fidelity of the numerical model.

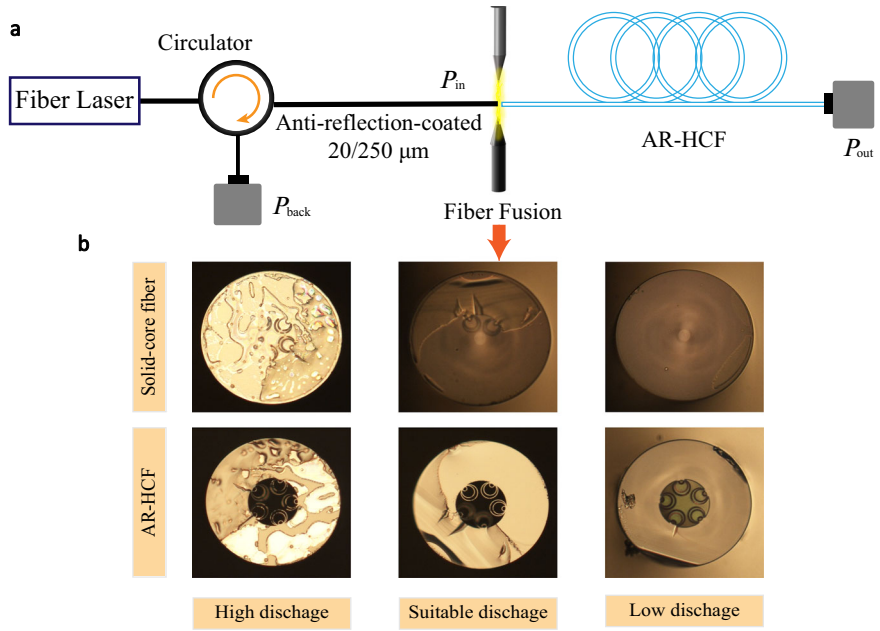

Fig. 2 | Fiber fusion splicing of the anti-reflection-coated SCFs and the AR-HCF. a The experimental setup of fusion splicing. **b** Cross-section views of post-splicing of SCFs and AR-HCFs at relatively high, suitable, and low discharge parameters.

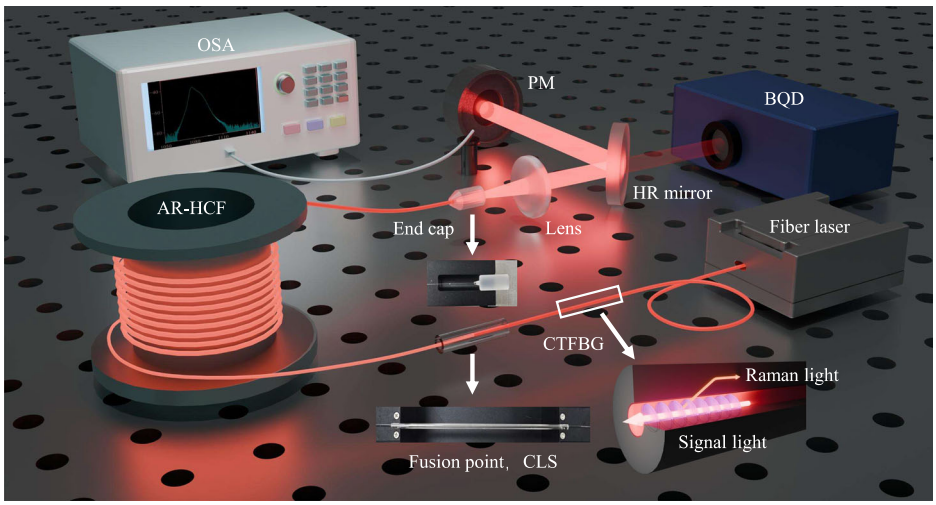

Fig. 3 | The experimental step of high-power laser delivery. OSA, optical spectrum analyzer; PM, power monitor; BQD, beam quality detector; HR mirror, high-reflection mirror; CTFBG, chirped and tilted Bragg grating; CLS, cladding light stripper. The insets show the practical maps of glass tube and end cap of AR-HCF, and the concept map of CTFBG.

Experimental system

Figure 3 shows the experimental setup for high-power laser delivery. (see Supplementary Note 4 for the photograph of the experimental step). A continuous- wave laser at 1080 nm was used as the source. A CTFBG was added after the laser source to suppress the Raman noise. The CTFBG was fabricated on a piece of 20/250 μm fiber and exhibited a Raman attenuation band spanning 1125 to 1150 nm (3 dB bandwidth of ~ 25 nm) with an attenuation depth exceeding 20 dB (see Supplementary Note 3 for the transmission spectrum of CTFBG). The output laser was delivered via an anti-reflection-coated SCF of 20/250 μm, and was subsequently fusion-spliced with the AR-HCF using the optimized parameters. To mitigate localized thermal damage during high-power operation, a 2-cm-long cladding light stripper (CLS) was implemented via chemical etching at the AR-HCF right after the fusion point. The fusion point and the CLS were positioned within a glass tube for stability and protection. To enhance optical fiber heat dissipation, the AR-HCF was wound onto an aluminum spool with a diameter of 320 mm and a height of 400 mm. In practical applications, the output terminal of AR-HCF is prone to contamination from dust, pollutants, or environmental moisture. To address this, we fused an anti-reflection-coated end cap at its output end for protection, which features a maximum diameter of 8.2 mm with an overall length of 20 mm. At the small end of it, the minimum diameter is designed to be 500 μm. The practical maps of glass tube and the end cap are shown in the insets of Fig. 3.

Observation of SRS in AR-HCF

Preliminary investigations were carried out utilizing a 200 m AR-HCF for high-power laser delivery, with no CTFBG employed in the setup. At an input power of 2400 W, spectral monitoring reveals characteristic peak at around 1142 nm that is considered to be the Stokes light generated by SRS in silica glass. However, the laser source output spectrum does not have obvious Raman spectral lines at the same power, as shown in

https://doi.org/10.1038/s41467-025-64073-y

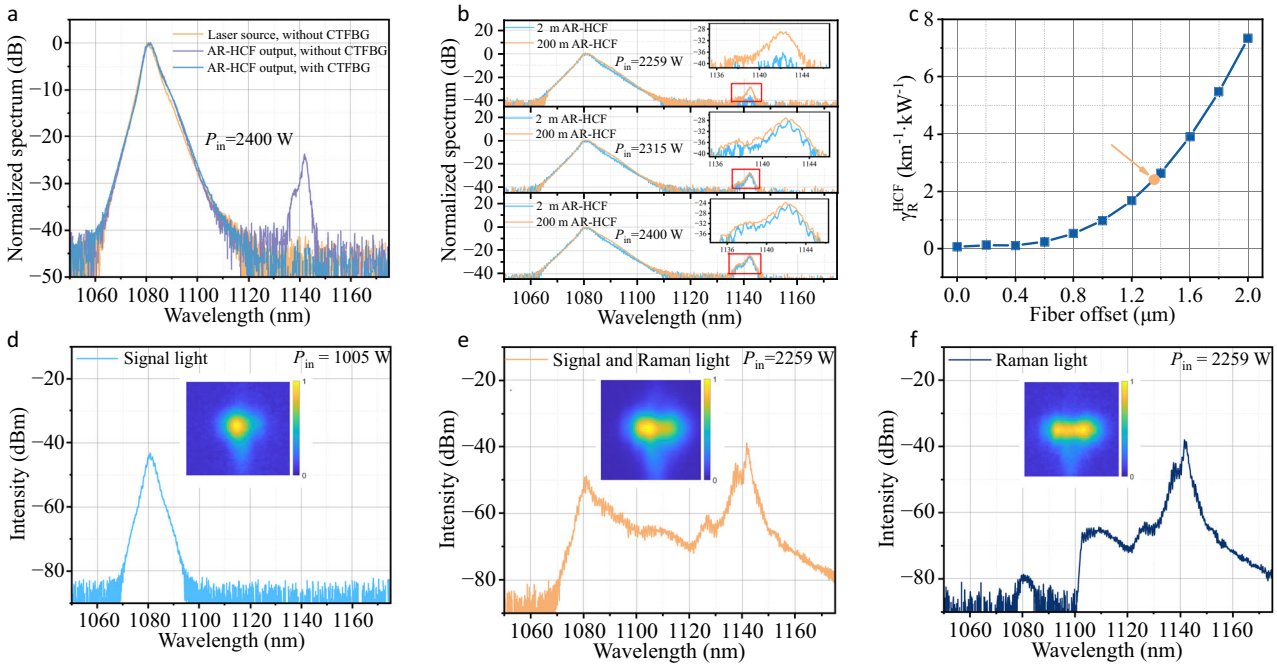

Fig. 4 | Experiment results of SRS in AR-HCF. a The normalized output spectra of laser source without CTFBG (orange line), 200 m AR-HCF without CTFBG (purple line) and with CTFBG (blue line) at 2400 W input power. **b** The normalized output spectra of 2 m (blue line) and 200 m (orange line) AR-HCF at 2259 W, 2315 W and 2400 W input power at the same fusion point between SCF and AR-HCF without CTFBG. The red boxes are enlarged areas. **c** Simulated the relationship between effective Raman gain coefficients and fusion offset. The orange arrow points to the effective Raman gain coefficient obtained from the experiment. Transmission spectra and beam profiles of (**d**), signal light at 1005 W input power, (**e**), signal and Raman light and (**f**), Raman light at 2259 W input power over a 2 m AR-HCF without CTFBG.

Fig. 4a. To determine whether SRS in AR-HCF originated from the internal Raman noise of laser source (which was not initially apparent in the spectrum), a CTFBG was spliced after the laser source. In contrast, the control group was spliced with the same length SCF of 20/250 μm with the CTFBG. Figure 4a shows the output spectra of a 200 m AR-HCF at 2400 W input power, comparing cases with and without the CTFBG. The SRS component disappears when the CTFBG was inserted. This confirms that internal noise from the laser source is a key for inducing Raman scattering in AR-HCF. Then, to investigate SRS amplification in AR-HCF, we compared laser spectra (without CTFBG) transmitted after 2 m and 200 m AR-HCF under the input powers 2259 W, 2315 W, and 2400 W. This comparison was performed with the same fusion point maintained between the SCF and AR-HCF. The corresponding results are shown in Fig. 4b. By integrating the spectra, we determined that at 2259 W input power, the SRS intensity after a 200 m AR-HCF transmission is 2.98 times higher than that after a 2 m transmission, confirming the accumulation of nonlinear effects. It is worth noting that under input powers of 2315 W and 2400 W, the SRS intensity of 200 m AR-HCF relative to 2 m AR-HCF decreased to 1.33 and 1.28 times, respectively. This reversal phenomenon is mainly due to the differential attenuation characteristics in AR-HCF: when the signal light experiences a transmission loss of 0.168 dB/km, the attenuation of the Raman component is higher with a transmission loss of 0.890 dB/km. Since the loss of AR-HCF to Raman light is higher than that of signal light, Raman growth is slower in longer fibers as the power increases. Additionally, the Raman light may propagate in higher-order modes, as observed in the spot profile in Fig. 4f, consequently exhibiting higher transmission loss. Based on the scaling ratio of SRS in the experiments, we calculated the effective Raman gain coefficient of AR-HCF as 2.4 $km^{-1} \cdot kW^{-1}$ (see Methods for the detailed definition and calculation).

Figure 4d–f show the signal and Raman beam profiles, and their corresponding spectra without CTFBG (see Methods for detailed measurement methods). At an input power of 1005 W, the beam profile of signal light predominantly consists of core light, as shown in Fig. 4d. When the input power is 2259 W, the signal light and Raman light simultaneously exist and exhibit a mixed mode within both the fiber core and the nested tubes, characterized by a more pronounced intensity within the core (Fig. 4e). The signal light and the Raman light were separated through two coated glass long-pass filters (see Supplementary Note 2 for transmission spectra). Figure 4f shows the spectrum and beam profile of only Raman light after filtering most of the signal light at an input power of 2259 W. It is discernible that Raman light exists in both core and nested tubes. The experimental results demonstrate that SRS originates in Raman noise stemming from the laser source, and is then amplified in the nested tube structure. Furthermore, fiber offsets during splicing can increase overlap between the optical field and nested tubes of AR-HCF, which in turn enhances the Raman gain. We simulated and calculated the effective Raman gain coefficients of AR-HCF varying with the fiber offset using FEA, and the results are shown in Fig. 4c. When the input laser is coupled into the fiber core without any deviation, the effective Raman gain coefficient is 0.05 km^{-1}·kW^{-1}. At a fiber offset of ~1.4 μm, the effective Raman gain coefficient increases sharply to 2.63 km^{-1}·kW^{-1}, which is close to experimental calculation results. This indicates a deviation of ~1.4 μm between the SCF and the AR-HCF at the fusion point. Furthermore, the effective Raman gain coefficient of the AR-HCF has a change due to various factors, including the precision of splicing alignment, the thickness of the nest tubes, the core diameter of AR-HCF and so on (see Supplementary Note 5 for simulation results).

High-power delivery in AR-HCFs

Drawing from the preceding analysis of SRS, we conducted a laser delivery by utilizing a CTFBG to mitigate the intrinsic Raman noise of laser source, as illustrated in Fig. 4. Figure 5 presents the high-power laser delivery results over 1 km and 2.45 km. The power delivery performances of 1 km and 2.45 km AR-HCF systems with and without end caps are shown in Fig. 5a. The left axes show the transmission efficiency and the corresponding output power vary with the input power of

https://doi.org/10.1038/s41467-025-64073-y

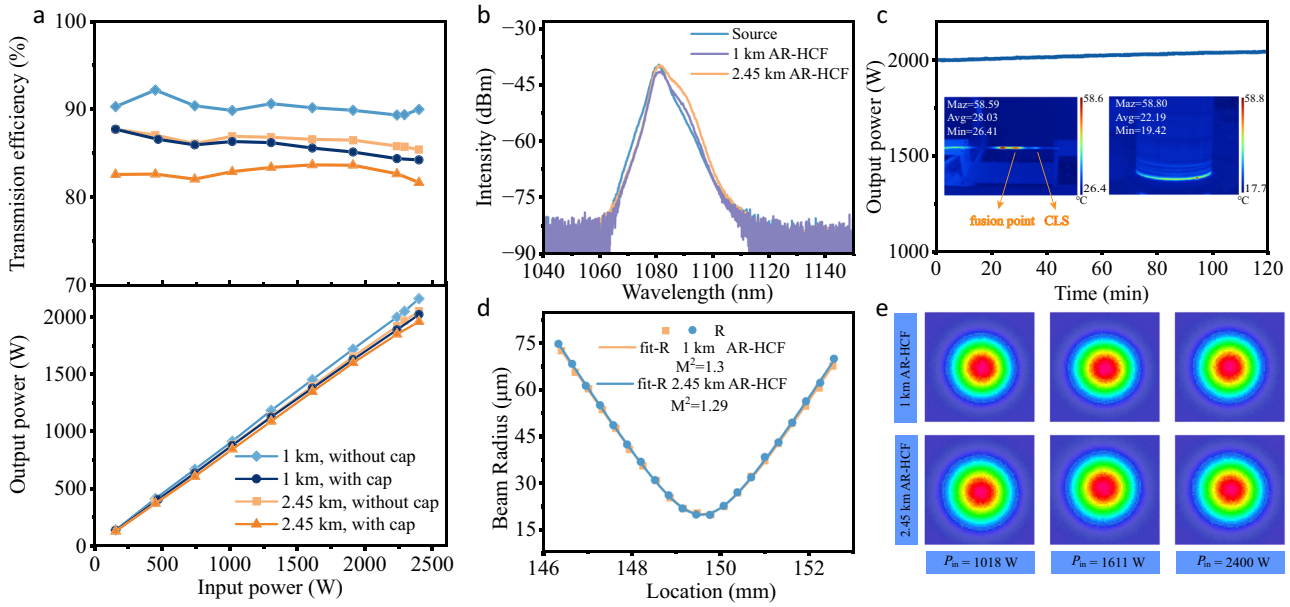

Fig. 5 | High-power laser delivery results. a Power delivery results after 1 km and 2.45 km transmission. **b** Input and output spectra after the 1 km and 2.45 km AR-HCF transmission at maximum input power; **c** 2-hour power test result of 1 km AR-HCF using end cap output at the maximum input power. The inset shows the thermal image of the fusion point, CLS and fiber spool at the maximum input power. **d** Measurement of beam quality factors of 1 km and 2.45 km AR-HCF at the maximum input power. **e** Beam profile diagram of AR-HCF at different input powers of 1018 W, 1611 W and 2400 W after transmitting through 1 km and 2.45 km AR-HCF, respectively.

AR-HCF. For 2.45 km AR-HCF, the maximum output power is 2050 W with a transmission efficiency of 85.4%, while the maximum output power after the end cap is 1960 W with a transmission efficiency of 81.7% at an input power of 2400 W. At the maximum input power of 2400 W, the 1 km AR-HCF delivers 2160 W with a transmission efficiency of 90.0%, which reduces to 2022 W with a transmission efficiency of 84.2% when an end cap is spliced. At the maximum input power, the coupling loss falls within the range of 0.27-0.29 dB, which has a marginal increase in comparison to the results obtained during low-power testing (~0.17 dB). Figure 5b shows the output spectra of the source, 1 km AR-HCF and 2.45 km AR-HCF at the maximum input power. The output spectra of the AR-HCF exhibit excellent consistency with the laser source spectrum, with no observable SRS nonlinear effects. The minor spectral redshift can be attributed to the Raman response of the atmospheric air within the core[25]. Figure 5c presents a 2-hour power test of the end cap output structure with a 1 km AR-HCF. Under maximum input power, the system exhibits a 2.3% power fluctuation, demonstrating excellent long- term stability. Meanwhile, Fig. 5c displays the thermal image of the coiled fiber and glass tube, which includes a fixed fusion point and the CLS. The highest temperature recorded in the glass tube is 58.59 °C. The hot spot in front of the fusion point is located at the interface between the cladding and coating of the SCF. The average temperature of the coiled fiber is 22.19 °C, but there are individual hotspots with temperatures of 58.8 °C. At maximum input power (2400 W), the laser source exhibits a beam quality factor (M^2) of 1.26. Corresponding measurements of the AR-HCF output (Fig. 5d) demonstrate excellent beam quality preservation, with M^2 values of 1.30 (1 km AR-HCF) and 1.29 (2.45 km AR-HCF) under identical power conditions. The near-field diffraction patterns of 1 km and 2.45 km AR-HCFs were systematically characterized under varying power levels, with measurements conducted at input powers of 1018 W, 1611 W, and 2400 W, as illustrated in Fig. 5e. The results demonstrate that as fiber length and power increase, the beam profiles consistently maintain a well-defined Gaussian distribution without significant degradation. This result demonstrates the capability of AR-HCFs to maintain beam quality over kilometer-scale distances at multi-kilowatt power levels, confirming their suitability for industrial and scientific high-power long-distance laser delivery systems.

Discussion

In this study, we report an integrated all-fiber laser delivery system based on AR-HCFs, which provides a robust solution to spatial coupling instability in high-power applications. Our self-fabricated AR-HCF features an optimized five-element double-nested architecture that achieves an ultralow transmission loss of 0.168 dB/km at 1080 nm, which represents the lowest reported value for this spectral band to date. Moreover, we developed an optimized splicing technique for AR-HCF and anti-reflection-coated SCFs, achieving a low average splicing loss (~0.17 dB) and an average return loss (~−28.5 dB) at an input power of 10 mW. Furthermore, the fusion point between anti-reflection-coated SCF and AR-HCF was fixed with glass tubes, and the output end was spliced with an end cap for protection. Consequently, a stable all-fiber high-power of 2 kW delivery system was achieved over a 2.45 km AR-HCF with a transmission efficiency of 85.4% through the above technologies. This advancement would surely facilitate the transition of AR-HCF technology from laboratory research to practical applications significantly.

Notably, the SRS amplified within the silica nested tubes of AR−HCF was observed for the first time in our experiments, which was caused by the amplification of the Raman noise stemming from laser source. This nonlinear effect is considered as a limiting factor for achieving higher power and longer transmission distance. Two suppression strategies are proposed: Firstly, Raman noise from the laser source can be effectively suppressed through a CTFBG, which has been validated in our experiments; Secondly, the AR-HCF can be designed to reduce the Raman gain. Simulations reveal significant correlations between structural parameters (fiber offset, nested tube thickness, and core diameter) and effective Raman gain coefficients (see Supplementary Note 5 for simulation results). In all-fiber architecture, as the

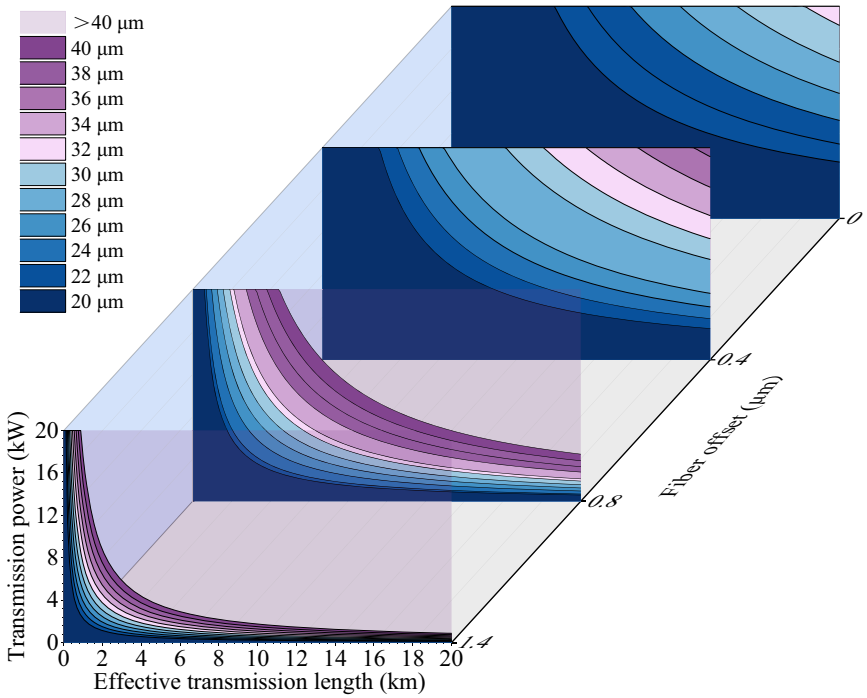

Fig. 6 | The scalability of continuous power transmission of AR-HCF in 1 μm spectral band, which is limited by SRS amplified within the silica nested tubes. The spectral profile was determined based on the standard approximation of the SRS critical power (see Methods). The different colors in the figure corresponds to the core diameter of AR-HCF. The orange pentagram represents the transmission power and effective transmission length corresponding to this work. Only the fundamental mode excitation is considered in the figure.

fiber offset increases, the effective Raman gain coefficient also increases. The thickness of nested tubes exhibits a nonlinear response characteristic with respect to the effective Raman gain coefficients. When the nested tube thickness deviates the signal wavelength from the resonance condition, the overlap integral between the optical field and the nested tube decreases, thereby inducing a smaller gain coefficient. The fiber core diameter is negatively correlated with the effective Raman gain coefficient, so the core size should be maximized in design under the condition of ensuring fundamental mode transmission. Figure 6 presents the achievable transmission distances as a function of output power for AR-HCFs with different core diameters and fiber offsets, limited by the SRS threshold criterion[36] (see Methods). AR-HCFs with a core diameter of 32 μm can achieve an effective transmission distance exceeding 20 km at 20 kW without fiber offset, while those with a 38 μm core diameter achieve this distance at the same power with a 0.4 μm offset. For larger offsets (0.8 μm and 1.4 μm), larger core diameters are required. Fiber offset and core diameter of AR-HCFs significantly affect the maximum transmittable power and achievable transmission distance in all-fiber laser systems.

Looking forward, the all-fiber integrated laser delivery system based on AR-HCFs not only exhibits significant application potential in fields requiring high-power long-distance laser delivery, such as industrial manufacturing[3], nuclear decommissioning[7] and laser drilling of oil[8], but also has substantial value in other fields. Firstly, the long-distance transmission limitations of single-frequency lasers imposed by stimulated Brillouin scattering (SBS)[37] can be addressed through the AR-HCF due to its low nonlinearity and transmission loss. Secondly, long-distance AR-HCFs enable novel particle acceleration through radiation pressure, building upon experimentally demonstrated particle levitation and guidance in hollow-core fibers[38]. Thirdly, a low-loss all-fiber gas cell is constructed in this work, enabling high-sensitivity gas detection[39]. Moreover, our results may inspire other applications of AR-HCFs, such as fiber communications, distributed sensing, and quantum optics[40–42].

Methods

AR-HCF loss measurement

The loss of AR-HCF in this study was measured using the cutback technique. The test source was a supercontinuum source, which was connected to a piece of 20/250 SCF as the launch fiber. The light source was coupled to an AR-HCF featuring a bending radius of 16 cm by employing the alignment function of the fusion splicer. Then the AR-HCF output was connected to the OSA using a bare fiber adapter. Firstly, the output spectrum was recorded using the 1080 m AR-HCF. The fiber was then cut to 20 m while maintaining identical emission conditions, and the output spectrum was measured again. The transmission loss was measured by comparing output spectra before and after fiber length reduction. We repeated the same operation to cut off 1060 m AR-HCF to 20 m. The loss curve for the AR-HCF in Fig. 1f represents the average of two separately conducted measurements.

AR-HCF simulation

The modes loss and coupling loss of AR-HCF were simulated by the finite-element analysis method. The fine mesh size of the air region was set to no more than one-third of the solved wavelength, while the mesh size of the background material was set to no more than one- eighth of the solved wavelength. Set the boundary conditions to a perfect matched layer. The refractive index of the air region is set as 1, and the refractive index of the background material is set as the refractive index of SiO_2. According to the dispersion for SiO_2, the calculated refractive index is 1.449 at 1080 nm based on Sellmeier formula.

Signal and Raman light beam profile measurement

The beam profiles of both the signal light and the Raman light were measured using a charge-coupled device (CCD). The output light from the AR-HCF was first collimated using a 100 mm focal-length plano-convex lens. Subsequently, a beam-splitting system composed of two high-reflectivity mirrors (HR mirrors) directed the majority of the beam energy served as a power attenuation mechanism (see Supplementary

Note 2 for transmission spectral line of HR mirrors), while the transmitted component was utilized for detection. The transmitted light was then focused by a 400 mm focal-length lens, with the CCD precisely positioned at the focal plane to capture the near-field diffraction pattern of the AR-HCF output. To accommodate dynamic power adjustment requirements, a tunable optical attenuator was incorporated upstream of the CCD to optimize the dynamic range of light intensity. The complete evolution of the beam profile under varying power conditions can be viewed in the supplementary. When testing only the Raman spot, two coated glass long-pass filters are used to isolate the Raman light (see Supplementary Note 2 for transmission spectral line of two filters).

Calculated method of Raman gain coefficient of AR-HCF

i. **Calculation based on experimental data**. We can calculate the Raman gain coefficient of AR-HCF using the coupled wave equation:

$$\frac{dI_R}{dz} = g_R I_S I_R - \alpha_R I_R \tag{2}$$

$$\frac{dI_S}{dz} = -\frac{\omega_S}{\omega_R} g_R I_S I_R - \alpha_S I_S \tag{3}$$

When $I_R \ll I_S$, the transmission loss of fiber (α_R, α_S) can be ignored. Therefore,

$$G_{HCF} = \exp(\gamma_R^{HCF} P_S L_{eff}) \tag{4}$$

$$L_{eff} = \frac{1 - e^{-\alpha_s L}}{\alpha_s} \tag{5}$$

$$\gamma_R = \frac{g_R}{A_{eff}} \tag{6}$$

$$G_{HCF} = \exp(\gamma_R^{HCF} P L - \alpha L) \tag{7}$$

Here, I_R and I_S denote the intensities of the Raman and signal light, respectively, while their corresponding angular frequencies are represented by ω_R and ω_S. The Raman gain characteristics are described by two coefficients: the Raman gain coefficient g_R and the effective Raman gain coefficient γ_R. α_S and α_R represent the transmission loss of signal light and Raman light. L_{eff} and L represent the effective interaction length and transmission length, respectively. A_{eff} is the effective mode field area. Experimental results demonstrate a total Raman gain $G_{HCF} \approx 2.98$ at a signal power (P_S) of 2259 W. With a signal attenuation $\alpha_S = 0.168$ dB/km and $L_{eff} \approx L = 0.2$ km, we derive an effective Raman gain coefficient $\gamma_R^{HCF} \approx 2.4 km^{-1} \cdot kW^{-1}$.

ii. **Calculation based on simulation results**. Furthermore, the Raman gain coefficient of AR-HCF can be determined using the Raman gain coefficient of the solid core fiber as a reference.

$$\gamma_R^{HCF} = \eta \frac{A_{eff}^{SCF}}{A_{eff}^{HCF}} \gamma_R^{SCF} \tag{8}$$

For the SCF of 20/250 μm, its mode field area is approximately 284 μm^2 (A_{eff}^{SCF}). The Raman gain coefficient of SCF[36] g_R is 10^{-13} km·kW^{-1} and γ_R^{SCF} is around 352 km^{-1}kW^{-1}. For the AR-HCF, SRS amplified within the silica nested tubes. And over 98% of the optical intensity is concentrated within approximately the outer quarter region of the outermost nested tubes based on FEA. Therefore, A_{eff}^{HCF} is approximated as quarter region of the outermost nested tubes, which is around 120 μm^2. The parameter η represents the ratio of the optical intensity localized in A_{eff}^{HCF} to the total optical intensity. This value was derived through FEA. Subsequently, γ_R^{HCF} is calculated. Based on analysis, the simulation of the effective Raman gain coefficient under various fusion offsets between SCF and HCF are conducted in the supplementary.

According to the definition of the SRS critical power - which refers to the state where the power at the signal wavelength and Raman wavelength reach equilibrium - its expression can be approximated as[36]

$$P_{cr} = \frac{16 A_{eff}}{g_R L_{eff}} = \frac{16}{\gamma_R L_{eff}} \tag{9}$$

According to the simulation calculation of γ_R(see Supplementary Note 4), the maximum transmission power and length can be calculated, as shown in Fig. 6.

Data availability

The processed data in this paper are available at https://doi.org/10.6084/m9.figshare.30031966.

References

1. Jauregui, C., Limpert, J. & Tünnermann, A. High-power fibre lasers. *Nat. Photonics* **7**, 861–867 (2013).
2. Nilsson, J. & Payne, D. N. High-power fiber lasers. *Science* **332**, 921–922 (2011).
3. Zervas, M. N. & Codemard, C. A. High power fiber lasers: A review. *IEEE J. Sel. Top. Quantum Electron.* **20**, 219–241 (2014).
4. Yang, B. L. et al. Monolithic fiber laser oscillator with record high power. *Laser Phys. Lett.* **15**, 75106 (2018).
5. Shima, K. et al. 5-kW single stage all-fiber Yb-doped single-mode fiber laser for materials processing. In *Proc. SPIE 10512, Fiber Lasers XV: Technology and Systems* (eds. Hartl, I. & Carter, A. L.) 105120C (SPIE, 2018).
6. Wang, Y. et al. 8-kW single-stage all-fiber Yb-doped fiber laser with a BPP of 0.50 mm-mrad. In *Proc. SPIE 11260, Fiber Lasers XVII: Technology and Systems* (ed. Dong, L.) 1126022 (SPIE, 2020).
7. Jae, S. S., Ki-Hee, S., Seong, Y. O. & Seung-Kyu, P. Laser cutting studies on 10–60 mm thick stainless steels with a short focus head for nuclear decommissioning. *Opt. Laser Technol.* **169**, 110121 (2024).
8. Zhang, S. Z. et al. Characterizing the laser drilling process of oil shale using laser-induced voltage. *Opt. Laser Technol.* **131**, 106478 (2023).
9. Wei, C., Joseph Weiblen, R., Menyuk, C. R. & Hu, J. Negative curvature fibers. *Adv. Opt. Photon.* **9**, 504 (2017).
10. Zhou, Z. et al. Towards high-power mid-IR light source tunable from 3.8 to 4.5 μm by HBr-filled hollow-core silica fibres. *Light Sci. Appl.* **11**, 15 (2022).
11. Sakr, H. et al. Hollow core optical fibres with comparable attenuation to silica fibres between 600 and 1100 nm. *Nat. Commun.* **11**, 6030 (2020).
12. Gao, S. et al. Fourfold truncated double-nested antiresonant hollow-core fiber with ultralow loss and ultrahigh mode purity. *Optica* **12**, 56–61 (2025).
13. Russell, P. Invited commentary: hollow core glass fibre-the perfect pipe for light. *eLight* **5**, 1–5 (2025).
14. Kolyadin, A. N. et al. Negative curvature hollow-core fibers: Dispersion properties and femtosecond pulse delivery. *Phys. Procedia* **73**, 59–66 (2015).
15. Poletti, F. Nested antiresonant nodeless hollow core fiber. *Opt. Express* **22**, 23807–23828 (2014).
16. Yu, F. et al. Attenuation limit of silica-based hollow-core fiber at mid-IR wavelengths. *APL Photonics* **4**, 080803 (2019).
17. Numkam Fokoua, E., Abokhamis Mousavi, S., Jasion, G. T., Richardson, D. J. & Poletti, F. Loss in hollow-core optical fibers: mechanisms, scaling rules, and limits. *Adv. Opt. Photon.* **15**, 1–84 (2023).
18. Belardi, W. & Knight, J. C. Hollow antiresonant fibers with low bending loss. *Opt. Express* **22**, 10091–10096 (2014).

19. Debord, B. et al. Ultralow transmission loss in inhibited-coupling guiding hollow fibers. *Optica* **4**, 209–217 (2017).
20. Gu, S. et al. Single-ring hollow-core anti-resonant fiber with a record low loss (4.3 dB/km) for high-power laser delivery at 1 μm. *Opt. Lett.* **47**, 5925–5928 (2022).
21. Jasion, G. T. et al. 0.174 dB/km Hollow Core Double Nested Anti-resonant Nodeless Fiber (DNANF). In *Optical Fiber Communication Conference 2022* (eds. Matsuo, S. et al.) paper Th4C.7 (Optical Society of America, 2022).
22. Chen, Y. et al. Hollow Core DNANF Optical Fiber with <0.11 dB/km Loss. In *Optical Fiber Communication Conference 2024* (eds. Fludger, C. et al.) paper Th4A.8 (Optical Society of America, 2024).
23. Petrovich, M. et al. Broadband optical fibre with an attenuation lower than 0.1 decibel per kilometre. *Nat. Photonics*. https://doi.org/10.1038/s41566-025-01747-5 (2025).
24. Sakr, H. et al. Hollow core NANFs with five nested tubes and record low loss at 850, 1060, 1300 and 1625nm. In *Optical Fiber Communication Conference (OFC) 2021* (eds. Dong, P. et al.) paper F3A.4 (Optical Society of America, 2021).
25. Mulvad, H. C. H. et al. Kilowatt-average-power single-mode laser light transmission over kilometre-scale hollow-core fibre. *Nat. Photonics* **16**, 448–453 (2022).
26. Cooper, M. A. et al. 2.2 kW single-mode narrow-linewidth laser delivery through a hollow-core fiber. *Optica* **10**, 1253–1259 (2023).
27. Yao, J. et al. High-Efficiency Distortion-Free Delivery of 3 kW Continuous-Wave Laser Using Low-Loss Multi-Mode Nested Hollow-Core Anti-Resonant Fiber. *J. Lightwave Technol.* **42**, 5710–5716 (2024).
28. Lekosiotis, A. et al. On-target delivery of intense ultrafast laser pulses through hollow-core anti-resonant fibers. *Opt. Express* **31**, 30227–30238 (2023).
29. Michieletto, M. et al. High-power picosecond pulse delivery through hollow core photonic band gap fibers. In *Workshop on Specialty Optical Fibers and Their Applications 2015* (ed. Ballato, J.) paper WF2A.4 (Optica Publishing Group, 2015).
30. Jones, D. C., Bennett, C. R. M., Smith, A. & Scott, A. M. High-power beam transport through a hollow-core photonic bandgap fiber. *Opt. Lett.* **39**, 3122–3125 (2014).
31. Gao, S. et al. All-fiber delivery of 100 W single-frequency laser through 100 m anti-resonant hollow-core fiber without stimulated Brillouin scattering. *High. Power Laser Sci. Eng.* **12**, e99 (2024).
32. Habib, Md. S., Antonio-Lopez, J. E., Markos, C., Schülzgen, A. & Amezcua-Correa, R. Single-mode, low loss hollow-core anti-resonant fiber designs. *Opt. Express* **27**, 3824–3836 (2019).
33. Shi, B. et al. Splicing hollow-core fiber with standard glass-core fiber with ultralow back-reflection and low coupling loss. *ACS Photonics* **11**, 3288–3295 (2024).
34. Zuba, V. et al. Limits of coupling efficiency into hollow-core anti-resonant fibres. *J. Lightwave Technol.* **41**, 6374–6382 (2023).
35. Wang, C. Y., Yu, R. W., Xiong, C., Zhu, J. & Xiao, L. M. Ultralow-loss fusion splicing between antiresonant hollow-core fibers and antireflection-coated single-mode fibers with low return loss. *Opt. Lett.* **48**, 1120–1123 (2023).
36. Agrawal, G. P. *Nonlinear Fiber Optics* 3rd edn (Academic, 2001).
37. Kobyakov, A., Sauer, M. & Chowdhury, D. Stimulated Brillouin scattering in optical fibers. *Adv. Opt. Photon.* **2**, 1–59 (2010).
38. Benabid, F., Knight, J. C. & Russell, P. S. J. Particle levitation and guidance in hollow-core photonic crystal fiber. *Opt. Express* **10**, 1195–1203 (2002).
39. Liu, D. et al. Highly sensitive twist sensor based on partially silver coated hollow core fiber structure. *J. Lightwave Technol.* **36**, 3672–3677 (2018).
40. Miele, E. et al. Hollow-core optical fibre sensors for operando Raman spectroscopy investigation of Li-ion battery liquid electrolytes. *Nat. Commun.* **13**, 1651 (2022).
41. Zhang, X. et al. Low-loss microwave photonics links using hollow core fibres. *Light Sci. Appl.* **11**, 213 (2022).
42. Wang, R. et al. Optical trapping of mesoscale particles and atoms in hollow-core optical fibers: principle and applications. *Light Sci. Appl.* **14**, 146 (2025).

Acknowledgements

The authors gratefully acknowledge support from the Science and Technology Innovation Program of Hunan Province (2021RC4027, Z.Z.). We would like to thank Yangmei Sun, Xiaoxi Liu, and Lianzhou Jiang for the sincere help and support on the fabrication and test.

Author contributions

Z.C., Z.W., and J.C. conceived the idea of the construction and methods for achieving all-fiber 2 kW laser delivery. J.S. and G.S. simulated the theoretical results. Z.X., P.L., Z.D., B.S. and L.Z. fabricated the AR-HCF. J.S., Z.C., B.R., and B.Y. assembled the setup and performed the measurements. J.S., Z.C., M.F, X.T., J.Z., and T.L. performed the power delivery, loss and M^2 measurements. Z.H. assisted in measuring the output beam profile. B.R and Z.Z. contributed to the interpretation of the experimental results. J.S. B.R., G.S., C.G., and Z.W. prepared the manuscript. Z.W. supervised this work and led the scientific collaboration.

Competing interests

The authors declare no competing interests.

Additional information

Supplementary information The online version contains supplementary material available at https://doi.org/10.1038/s41467-025-64073-y.

Correspondence and requests for materials should be addressed to Zilun Chen, Zefeng Wang or Jinbao Chen.

Peer review information *Nature Communications* thanks Francesco Poletti, who co-reviewed with Viktor Zubaand the other, anonymous, reviewers for their contribution to the peer review of this work. A peer review file is available.